Design of a multi-spectral imager built using the compressive sensing single-pixel camera architecture

Lenore McMackin, Matthew A. Herman, Tyler Weston
InView Technology Corporation, 6201 E. Oltorf Street, Austin TX 78741

ABSTRACT

We present the design of a multi-spectral imager built using the architecture of the single-pixel camera. The architecture is enabled by the novel sampling theory of compressive sensing implemented optically using the Texas Instruments DLP™ micro-mirror array. The array not only implements spatial modulation necessary for compressive imaging but also provides unique diffractive spectral features that result in a multi-spectral, high-spatial resolution imager design. The new camera design provides multi-spectral imagery in a wavelength range that extends from the visible to the shortwave infrared without reduction in spatial resolution. In addition to the compressive imaging spectrometer design, we present a diffractive model of the architecture that allows us to predict a variety of detailed functional spatial and spectral design features. We present modeling results, architectural design and experimental results that prove the concept.

Keywords: compressive sensing, multi-spectral imaging, digital micromirror device, blazed diffraction grating, shortwave infrared, Fourier diffraction theory, imaging spectrometer, Texas Instruments DLP

1. INTRODUCTION

Compressive Sensing (CS) is an innovative data sampling strategy[1] whose mathematical foundation exploits the property that signals and images are often sparse in some transform basis. By sampling in the correct transform space, we can recover high-quality images from far fewer measurements[2] than required by traditional Nyquist sampling rules.

We note here that the compressive data vector (and CS techniques in general) can be used for purposes other than imaging and in fact CS has found utility in machine vision analysis in data intensive applications such as gene microarrays[3,4], proteomics[5], and neuronal information processing[6]. In this paper we concentrate on the imaging application where exploiting sparsity allows us to perform high resolution imaging without requiring a high resolution pixel array. In the shortwave infrared regime this has particular advantages because high-resolution InGaAs focal plane arrays are not readily available.

InView Technology Corporation has implemented the principles of CS in a high-resolution shortwave infrared camera[7,8] based on the “single-pixel camera” architecture[9]. By modifying this architecture only slightly, we have extended the camera to a multispectral system capable of simultaneously imaging at a number of wavebands spanning the visible to shortwave infrared, leading to the creation of pseudo-color images without any reduction in spatial resolution usually associated with color imaging. In the following sections we discuss the single-pixel camera architecture. We develop a model of the camera’s optical path that shows the key element in the simple design of the multi-spectral camera is the Texas Instruments DLP™ micromirror array (DMD). By examining its interesting diffractive properties we show how these properties can be used to design a multi-spectral CS camera.

2. BACKGROUND ON THE COMPRESSIVE SENSING ARCHITECTURE

The architecture of the InView camera along with the procedure for constructing an image is shown Fig. 1. In traditional digital imaging, the camera lens images a scene onto a pixel array comprising a dense grid of tiny detectors. The signal from each pixel is read out, digitized and assembled such that each pixel represents one resolution element of the image. In contrast, only one detector is used in the CS architecture, onto which light from the entire field of view is integrated.

A CS data vector is formed by imaging the scene (1) onto a spatial light modulator and modulating it with a series of binary spatial patterns (2). The spatially modulated image is focused onto a detector (3) and an intensity measurement for each modulation pattern in the series is recorded (4) forming a data vector. CS theory dictates that we can obtain a data vector that is much shorter than data streams read out from pixel arrays of traditional cameras, and still encodes all the information of the scene. An image is then computed (5) by using the data vector to solve[10] a linear programming problem.

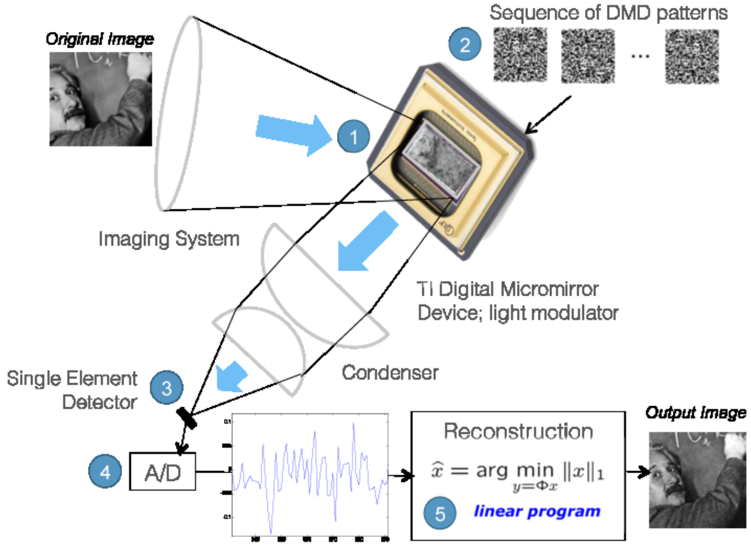

Fig. 1. Compressive sensing single-pixel camera architecture

An important aspect of the design of a compressive camera, and particularly the multi-spectral camera is the position, size and shape of the focused spot at the detector plane. Looking closely at the light appearing at the focal plane of the single-pixel camera, we see that the DMD not only imparts spatial patterns on the image but it also diffracts light into arrangements that are strongly dependent on wavelength, as illustrated by photographs in Fig. 2 taken of the DMD focal plane for various shortwave infrared wavelengths. In Fig. 3 focal plane properties of the light calculated from a diffractive model of the DMD at the same wavelengths are shown.

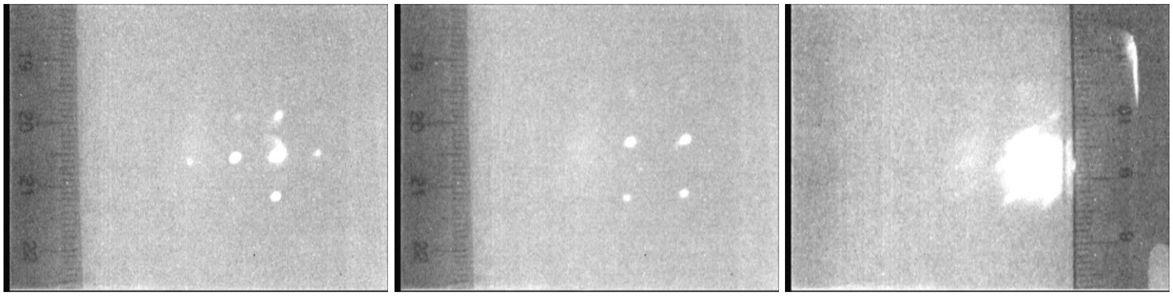
(a) (b) (c)

Fig. 2. Experimental photographs of the diffraction patterns modeled in Fig.3 at (a) 1250nm, (b) 1550nm, and (c) wideband 900-1700nm showing excellent agreement. Note that the photos are taken using a commercially available monochromatic IR camera so pictures appear only in black and white.

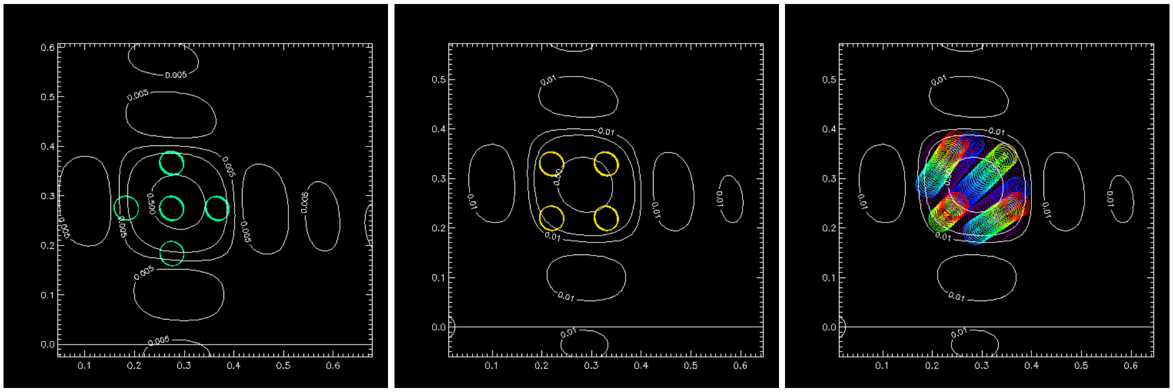

(a) (b) (c)

Fig. 3. Modeled diffraction patterns appearing at the detector plane of the CS camera architecture at SWIR wavelengths of (a) 1250nm, (b) 1550nm, and (c) wideband 900-1700nm. Contours of the blaze function are shown in white and take the form of a two-dimensional sinc function, which is the Fourier transform of an individual square micromirror.

We will describe the Figs. 2 and 3 in more detail after presenting the theoretical model. However, it is evident that the DMD performs two functions in the compressive camera architecture. First, it provides for the spatial modulation of an incident image with a set of encoding patterns that allow for compressive imaging. Additionally, due to the array's action as a switchable blazed diffraction grating[11], the array also imparts the modulated image's wavelength and spatial frequency information into a number of blazed diffraction orders of the array. These diffracted orders are closely spaced (we will show that all blazed orders are all roughly contained within the central lobe of a function with a sinc profile), and often overlap. For a monochromatic compressive camera it is sufficient to place at the focal plane one detector large enough to intercept the central lobe of the blaze function and the orders contained within it. The design of a spectral imager, however, requires the light to be dispersed by wavelength onto separate detectors that make similar compressive measurements at a variety of wavelengths. One way to perform this dispersion is to replace the single detector with the entrance aperture of a fiber-coupled spectrometer.[12,13] The fiber tends to integrate the structure of the blazed orders, while the remaining spectrometer optics disperses the light spectrally onto a linear detector array. Because the compressive encoding of the light is not affected by the spectrometer optics, each pixel can be used as an individual single-pixel camera to construct an image corresponding to its spectral component. While offering a way to perform hyperspectral imaging, this system requires mating the compressive camera front end to an optical spectrometer or spectrum analyzer by means of an aperture that restricts the numerical aperture and ultimately limits the spatial resolution of the image. The multi-spectral system we describe here uses both the compressive modulation and the diffractive order structure provided by the DMD resulting in a much simpler system, which –while not hyperspectral– provides several simultaneous wavebands for multi-spectral or "color" imaging without reduction in spatial resolution.

The main modification to the usual single-pixel architecture is the addition of a diffraction grating placed after the DMD and in front of a focusing lens as shown in Fig. 4. The blazed diffraction orders of the DMD are then further diffracted by the grating resulting in the angular dispersion by wavelength of the various blazed orders. Since the blazed orders themselves have only a limited waveband, the additional dispersion creates a convenient spatial separation of the diffracted orders. This separation makes each of these orders along with their spatial and wavelength information individually accessible to a number of individual detectors each of which can be used to compressively sense the data required for imaging at a particular waveband.

In order to design a spectral imager, a quantitative understanding of the diffractive behavior of the DMD is needed. In the following section, we summarize a diffractive model of the DMD using Fourier theory, calculate the distribution of light appearing at the detector plane of the CS camera architecture, and show the optical effect of an additional grating. We then describe the design of a detector that takes advantage of these behaviors for multi-spectral compressive imaging.

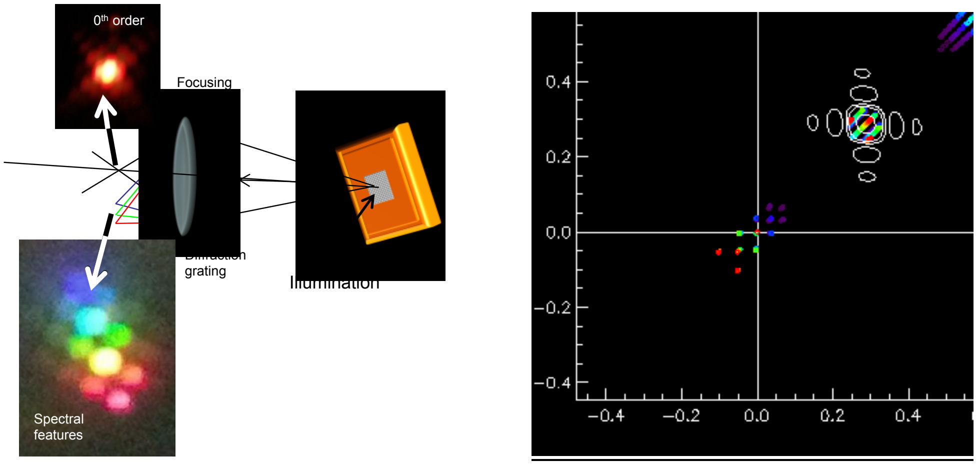

(a) (b)

Fig. 4. (a) The diagram shows photographs of the distribution of visible light at the focal plane of a lens that focuses light exiting the DMD and then further diffracted by a one-dimensional diffraction grating. The 0th order light undiffracted by the grating (top) shows the typical blaze function of the DMD. The grating disperses the various orders into their component colors (bottom). (b) shows the distribution of visible light at the same plane calculated from our model.

3. OPTICALLY MODELING BLAZED DIFFRACTION FROM MICROMIRRORS

In a general analysis, an illuminated array of micromirrors comprising the DMD can be modeled as the convolution of a rectangular mirror shape with an infinite two-dimensional comb function, times an illumination function that contains image information. An illustration of the micromirror array geometry used in this analysis is shown in Fig. 5.

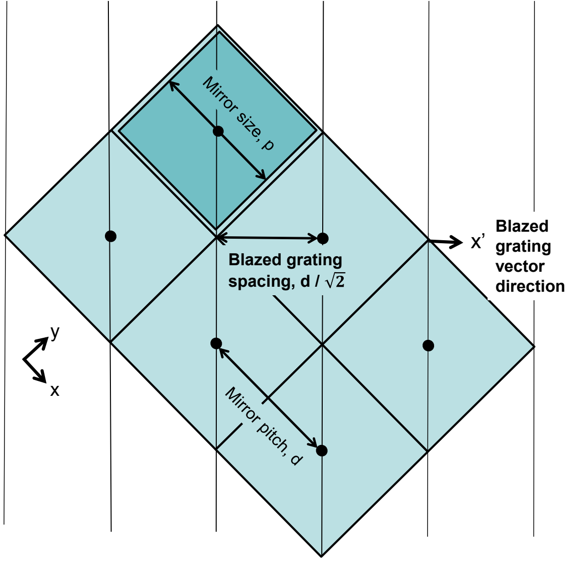

Fig. 5. Geometry of the DMD mirror array modeled in Eq. 1. The array is shown rotated at 45 degrees relative to the sides of the micromirrors to emphasize the geometry of the blazed diffraction grating produced by the mirror tilt. In this figure, the mirrors tilt about axes defined by the vertical lines. These vertical lines also define the spacing of the blazed grating produced by mirror tilt.

Following Goodman's[14] notation, the illumination function just after the DMD can be written,

$$g(x,y) = a(x,y)\left[rect\left(\frac{x}{p}\right) rect\left(\frac{y}{p}\right) \otimes comb\left(\frac{x}{d}\right) comb\left(\frac{y}{d}\right)\right] \qquad (1)$$

where $a(x,y)$ is the illumination function (in this case, it is the product of the image incident on the DMD and the CS modulation pattern), d is the DMD mirror spacing, p is the size of a DMD mirror as shown in Fig. 5, and the special rect and comb functions are given by:

$$\mathrm{rect}(z)=\begin{cases} 1 & |z|<\frac{1}{2} \\ \frac{1}{2} & |z|=\frac{1}{2} \\ 0 & \text{otherwise} \end{cases} \quad , \quad \mathrm{comb}(z)=\sum_{n=-\infty}^{\infty}\delta(z-n)\, , \tag{2}$$

where δ is a delta function and n is an integer. After diffraction from the DMD, light travels to the far field and will be distributed per the Fourier transform of the illumination at the DMD. Thus, by the convolution theorem, at the far field the illumination function $G(f_x,f_y) = \mathcal{F}\{g(x,y)\}$ can be written:

$$G(f_x,f_y) = p^2d^2A(f_x,f_y)\otimes[\mathrm{comb}(df_x)\mathrm{comb}(df_y)\mathrm{sinc}(pf_x)\mathrm{sinc}(pf_y)], \tag{3}$$

where f_x and f_y are spatial frequency variables and ⊗ is the convolution operator. Note that the comb function,

$$\mathrm{comb}(df_x) = \sum_{-\infty}^{\infty}\delta(\,df_x - m) \tag{4}$$

is non-zero only when $f_x = m/d$, for arbitrary integer m, and the sinc function

$$\mathrm{sinc}(pf_x) = \frac{sin(\pi pf_x)}{\pi pf_x} \tag{5}$$

peaks at $f_x = 0$. The central lobe of the sinc serves as an overall intensity modulation envelope of the infinite two-dimensional comb.

Equation 3 describes the far-field diffraction pattern created by the micromirror array geometry when the mirrors are not tilted. It represents set of diffracted orders $m = 0, \pm1, \pm2$ etc. appearing within a sinc envelope whose width is a function of the mirror size. The convolution indicates that the Fourier spectrum of the illumination function, $A(f_x,f_y)$, is replicated at each of these orders. Since the micromirrors tilt, they are able to controllably direct optical energy into a different set of orders, m, in a process called *blazing*. Mathematically, this tilt, represented by angle ϕ', introduces a linear phase term multiplying the *rect* function. For simplicity, we adopt the one-dimensional notation shown in Fig. 6, where the dimension x' is oriented along the direction perpendicular to the axis of mirror tilt. Eq. (1) can be re-written in the tilted case as

$$g(x') = a(x')e^{-ik_0x'\sin\theta_i}\left[\left[\mathrm{rect}\left(\frac{x'}{p\cos\phi'}\right)e^{i2k_0x'\sin\phi'}\right]\otimes\mathrm{comb}\left(\frac{x'}{d}\right)\right]\mathrm{rect}\left(\frac{x'}{D}\right). \tag{6}$$

where the axis x' is the direction along the grating vector direction indicated in Fig. 5, $k_0 = 2\pi/\lambda$, and $p\cos\phi'$ is the effective size of the micromirror tilted by angle ϕ' measured with respect to the array normal. In Eq. 6, the illumination is represented in general by a tilted wavefront $a(x')e^{-ik_0x'\sin\theta_i}$, and an additional *rect* term has been added to represent the full width of the DMD along x'. These parameters are shown in the diagram of the one-dimensional case in Fig. 6.

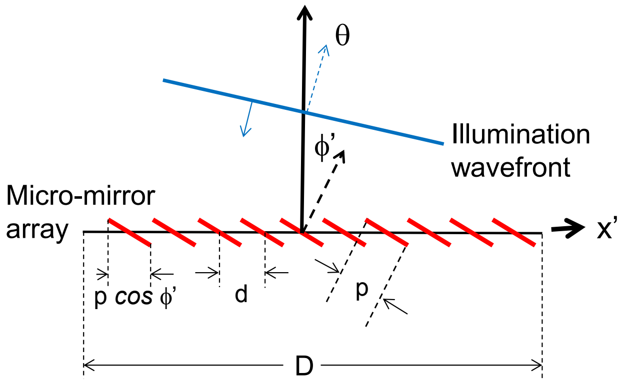

Fig. 6. One dimensional geometry of the DMD micromirror array. The illumination wavefront travels at angle θ_i with respect to the DMD normal. The tilt angle of the micromirrors is ϕ'

Equation 6 shows that the DMD grating can be represented as the convolution of a mirror "unit cell" and a comb function that replicates the unit cell along the extent D of the DMD. Mirror tilt acts to advance the wavefront's optical phase by an amount $2k_0 x' \sin\phi'$ over the width of the mirror. Transforming this expression for the blazed array to the far field yields

$$\mathrm{G}(f) = \mathrm{D\,d\,p}\cos\theta_i\,[\mathrm{G}_1] \otimes [\mathrm{G}_2] \tag{7}$$

with

$$\mathrm{G}_1 = \mathrm{A}(f) \otimes \mathrm{sinc}(f\mathrm{D}) \tag{8}$$

and

$$\mathrm{G}_2 = \delta\left(f + \frac{k_0 \sin\theta_i}{2\pi}\right) \otimes \mathrm{comb}(\mathrm{d}f)\left[\delta\left(f - \frac{2k_0 \sin\phi'}{2\pi}\right) \otimes \mathrm{sinc}(\mathrm{p}\,f\cos\phi')\right]. \tag{9}$$

G_1 can be identified as the spatial frequency spectrum of the CS-modulated image content that is low-pass-filtered by convolution with a narrow sinc function whose width is inversely proportional to the width of the full width of the micromirror array. Since D >> p, the sinc function is essentially a delta function and does not appreciably modify the image information content.

The G_2 term can be identified as the diffraction pattern resulting from the grating structure of the micromirror array, *blazed* by the tilt of the mirrors. To show this identification, we re-write Eq. 9 taking advantage of the convolution and shift properties of delta functions while also using the angular spectrum notation to express spatial frequency coordinate f as a function of angle, ζ, and wavelength λ,

$$\mathrm{f} = \sin\zeta \,/\, \lambda \tag{10}$$

to obtain

$$\mathrm{G}_2 = \mathrm{sinc}\left(\frac{\mathrm{p}\cos\phi'}{\lambda}(\sin\zeta + \sin\theta_i - 2\sin\phi')\right)\mathrm{comb}\left(\frac{\mathrm{d}}{\lambda}(\sin\zeta + \sin\theta_i)\right). \tag{11}$$

From Eq. 11, we see that the diffraction orders of the DMD grating occur where the argument of the comb function is an integer n, or at angles satisfying

$$\sin\zeta + \sin\theta_i = \mathrm{n}\frac{\lambda}{\mathrm{d}}\ , \tag{12}$$

which is the familiar grating equation, while the sinc function serves as an envelope. In the case of tilted mirrors, the peak of the sinc function is offset from the zeroth order of the grating by angle $2\phi'$. Mirror tilt thus translates the sinc blaze function envelope away from the zeroth order by an angle equal to the specular reflection angle from the DMD mirrors.

Finally, in $[G_1] \otimes [G_2]$ the convolution of the Fourier transform of the illumination function, *A*, with the comb and (blaze-displaced) sinc modulation will place a copy of *A* at each of the locations of the comb. Therefore, *A*, which is the spatial frequency spectrum of the illumination function, is repeated at each diffracted order in the far-field pattern in accordance with the Whittaker-Shannon sampling theorem. The intensity of each copy of *A* is also modulated by the amplitude of the sinc blaze function at its location.

Since the DMD mirrors can be oriented in one of two positions (e.g., ±12 degrees), there will be, in general, two sinc functions that modulate the infinite comb, one centered at each of the specular mirror angles. Figure 6 shows the far-field intensity for uniform illumination of a DMD that has roughly half its mirrors randomly oriented to each of the two tilt states. The result shows the fully realized sinc modulation envelope that occurs for each of the two mirror tilt positions. Note that the two sinc envelopes are not centered on any diffraction order, and that their zeroes have intervals that are slightly larger than the spacing of the diffraction orders, indicating that the DMD mirrors are slightly smaller than their spacing (as they must be to allow movement).

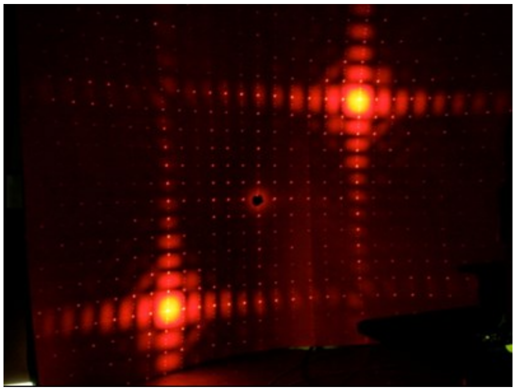

Fig. 7. Photograph of the far-field intensity for λ=0.633um light reflecting from a uniformly-illuminated DMD with mirrors evenly and randomly distributed between the two states of tilt

Figure 7 illustrates a number of important points regarding the diffraction pattern resulting from the DMD. We see in the background, the dim two-dimensional *comb* function of the DMD's diffracted orders. The comb spacing is set by the mirror pitch and the wavelength and does not change when the mirrors are tilted. What does change with mirror tilt is the position of the blaze function. Since the majority of the optical energy diffracts into the direction of the blaze function, only those diffracted orders of the array that are encompassed by the blaze function "light up." Depending on the wavelength of the illumination and mirror size, one or more diffracted orders may be blazed. In certain cases of mismatched mirror size and wavelength, no diffracted orders are blazed resulting in low efficiency.[15]

As seen in Fig. 7, whether these orders fill the blaze function depends on the spatial frequency spectrum, *A*, that surrounds each order. The figure illustrates the case of uniformly illuminating the DMD on which a random pattern of on and off mirrors is displayed. The Fourier transform of a uniform band-limited random pattern has equal power at all spatial frequencies up to the band limit. So in this case of randomly oriented mirrors, *A* is constant over all Fourier space, and essentially "fills up" the sinc modulation envelopes. In general, whether light actually fills the blaze function depends on a number of characteristics of the illumination that we illustrate in the Appendix.

With this understanding of the diffractive behavior of the DMD, we continue our mathematical modeling by examining the case where light diffracted from the DMD is then transmitted through a diffraction grating. We represent the grating with a sinusoidally varying transmission with modulation depth β and period t,

$$s(x') = 1 - \frac{\beta}{2}\cos\left(\frac{2\pi x'}{t}\right) - \frac{\beta}{2}. \tag{13}$$

Notice that the grating vectors of the sine grating and the DMD are both oriented along x′. After diffraction from the DMD grating and transmission through the sinusoidal grating Eq. 6 can be written

$$g(x') = a(x')e^{-ik_0 x' \sin\theta_i}\left[\left[\mathrm{rect}\left(\frac{x'}{p\cos\phi'}\right)e^{i2k_0 x' \sin\phi'}\right]\otimes \mathrm{comb}\left(\frac{x'}{d}\right)\right]\mathrm{rect}\left(\frac{x'}{D}\right)\left[1-\frac{m}{2}\cos\left(\frac{2\pi x'}{t}\right)-\frac{m}{2}\right] \quad (14)$$

Transforming this to the far field, we obtain an expression that may be written as

$$G(f) = D\, d\, p\cos\theta_i\,[G_1]\otimes[G_2]\otimes[G_3], \quad (15)$$

with G_1 and G_2 identified with the modulated image content and the DMD grating, respectively, and G_3

$$G_3 = \left(1-\frac{m}{2}\right)\delta(f) - \frac{m}{4}\left[\delta\left(f-\frac{1}{t}\right)+\delta\left(f+\frac{1}{t}\right)\right], \quad (16)$$

Convolving G_3 with the G_2 term yields

$$\begin{aligned} G_2\otimes G_3 = {} & \left(1-\frac{m}{2}\right)\mathrm{sinc}\left(\frac{p\cos\phi'}{\lambda}(\sin\zeta+\sin\theta_i-2\sin\phi')\right)\mathrm{comb}\left(\frac{d}{\lambda}(\sin\zeta+\sin\theta_i)\right) \\ & +\frac{m}{4}\mathrm{sinc}\left(\frac{p\cos\phi'}{\lambda}\left(\sin\zeta+\sin\theta_i+\frac{\lambda}{t}-2\sin\phi'\right)\right)\mathrm{comb}\left(\frac{d}{\lambda}\left(\sin\zeta+\sin\theta_i+\frac{\lambda}{t}\right)\right) \\ & +\frac{m}{4}\mathrm{sinc}\left(\frac{p\cos\phi'}{\lambda}\left(\sin\zeta+\sin\theta_i-\frac{\lambda}{t}-2\sin\phi'\right)\right)\mathrm{comb}\left(\frac{d}{\lambda}\left(\sin\zeta+\sin\theta_i-\frac{\lambda}{t}\right)\right). \end{aligned} \quad (17)$$

Convolving Eq. 17 with the G_1 term places a copy of the filtered Fourier transform of the image at each of the three copies of the grating orders. The sine grating diffracts the blaze function and the orders of the DMD contained within it into 0th, +1 and –1 orders, i.e., the first, second and third terms of Eq. 17, respectively. It is important to note that the +1 and –1 orders are not entirely symmetrical about the 0th order. We will examine $G(f)$ numerically in the next section.

4. NUMERICAL EVALUATION OF DMD DIFFRACTION

We tested and experimentally verified our model by implementing the full diffraction model of the CS camera's optical path numerically in two-dimensions in software that graphically represents the results.[16] The software calculates and displays the resulting diffraction pattern in a direction cosine (DC) space framework.[17] In a DC diagram, any unit vector can be represented as a point in a two-dimensional plot whose horizontal and vertical axes are the DCs of the vector's x- and y-axis components, respectively. Here, we use the DC diagram to visualize the diffraction patterns from the combination of the two-dimensional DMD and an additional one-dimensional grating based on a variety of inputs including micromirror size and spacing, tilt angle, and array orientation, and also f-number of the optical illumination. Our model allows visualization of the diffraction pattern and also calculation of the spectral content of light encircled by a detector of chosen size placed anywhere within the DC field.

Figure 8 shows a DC space representation of the far-field intensity of visual light diffracted from the DMD. The full DC space unit circle is shown in Fig. 8(a), with the DMD blaze function associated with one mirror tilt position appearing in the upper right quadrant along the grating vector direction (coincident with the mirror tilt direction) at 45 degrees. The sinc envelope of Eq. 11 defines the boundaries of the blaze amplitude, outside of which very little optical energy is diffracted. The close-up of the blaze function in Fig. 8(b) shows that the five different diffracted orders appearing within the blaze function are slightly dispersed along the grating vector direction indicating the spectral bandwidth associated with each of the orders. Figure 8(c) shows a photograph of the blazed diffraction from a DMD in visible light.

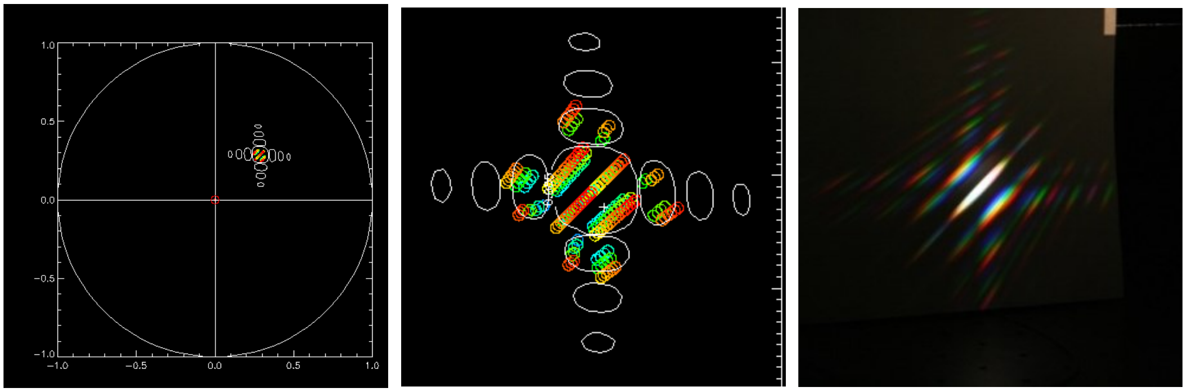

(a) (b) (c)

Fig. 8. DC space visualizations from DCLab™ showing (a) the entire unit circle representing DC space, and (b) a close up of the blaze function containing diffraction orders for n = 5 through 10 for visual wavelengths between λ = 500 and 700 nm. A photo of real blazed diffraction from a DMD in visible light is shown in (c).

More detail on the distribution of orders at within the blaze function at shortwave IR wavelengths can be seen in Fig. 3. Figures 3(a) and 3(b) show that the number of blazed orders as well as their position under the blaze function changes profoundly with wavelength. At 1250nm there are five distinct diffracted orders of the micromirror array that appear under the blaze function while at 1550nm there are four different orders. Under wideband illumination, shown in Fig. 3(c), all of these orders can be seen in combination with the waveband of each order represented by the slight spectral smearing of each order along the grating vector direction. These modeled results compare favorably to photographs of actual diffraction patterns, shown in Fig. 2, that are created at the same wavelengths.

The previous analysis reveals that the diffracted orders of the DMD and their wavelength components are closely grouped under the blaze function. Dispersion provided the additional diffraction grating spreads out the orders and makes them accessible to separate detectors in a CS camera. Figure 9 shows the dispersed far-field distribution model and corresponding experiment for shortwave IR light including wavelengths from 700-1600nm dispersed by a 2um spaced grating. We note that the dispersed light appears in an asymmetrical pattern on either side of the grating's 0th order (shown surrounded by the blaze function contour in Fig. 9). The asymmetry is a result of the sign differences between the second and third terms of Eq. 17. We note further that the more compact spectral features shown in the lower left diffracted order (+1) of the grating are the most useful for CS spectral imaging.

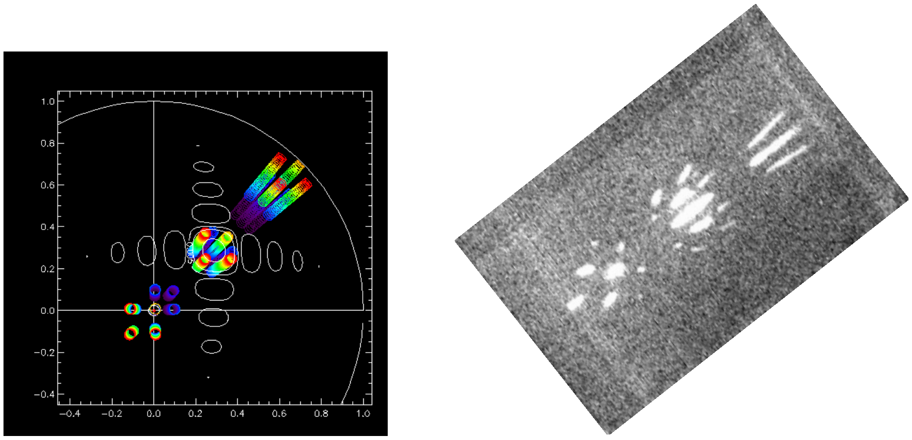

by

(a) (b)

Fig. 9. (a) Model of the micromirror array diffraction pattern dispersed by a second grating added to the optical path. The grating produces asymmetrical diffraction on either side of the central blaze function. (b) Photo of the SWIR pattern produced by the experimental system showing the blaze pattern in the center, and asymmetric spectral groups to the left and right.

5. DESIGN OF A VISIBLE-SHORTWAVE IR MULTI-SPECTRAL COMPRESSIVE CAMERA

We return now to the compressive camera architecture of Fig. 1 and how to incorporate the diffractive features shown in Fig. 4 to create a multi-spectral compressive camera. We concentrate on hardware modifications to InView's current (monochromatic) CS microscope camera necessary to implement the spectral imaging system, which consist of placing a grating in the optical path after the DMD and designing a multi-channel detector to measure several spectral features at the focal plane. A concept for the multi-spectral camera is shown in Fig. 10.

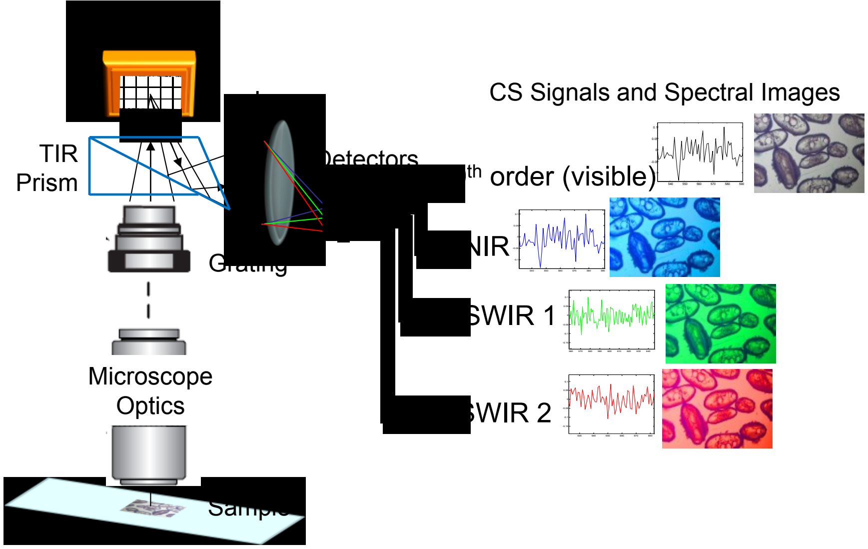

Fig. 10. In this multi-spectral CS imaging system, a microscope objective and tube lens image a sample onto the DMD. A total internal reflection (TIR) prism directs the modulated light from the DMD through a grating and focusing lens. The data vector measured from each of a set of discrete detectors placed at the focal plane can be reconstructed into an image using an algorithm designed for compressive sensing.

An interesting case arises at three wavebands in the near and shortwave infrared. At wavelength ranges 750-800nm, 930-1000nm and 1250-1370nm, only one diffracted order appears within the blaze function, centered so that diffraction efficiency is highest. After passing through grating the orders at these wavelengths are dispersed spatially as shown in Fig. 11(a), where the undiffracted 0th order of the grating is located at the upper right (shown with the blaze function outline) and the dispersed light shown diagonally along the grating vector direction.

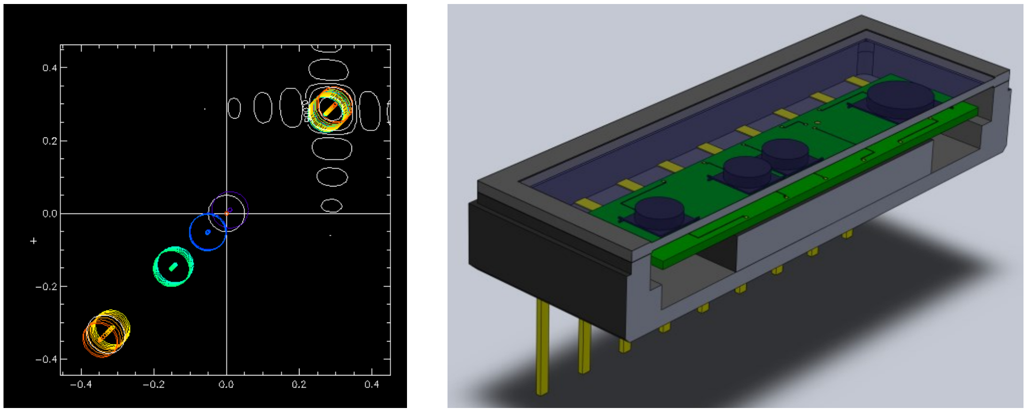

(a) (b)

Fig. 11 (a) DC space model of infrared wavelengths at which there is only one blazed diffracted order of the DMD. These wavelengths are convenient to use in the design of a detector for a multi-spectral CS camera because of high diffraction efficiency and compact spatial localization of the diffracted orders. (b) Multi-photodetector package designed to measure these wavebands.

We designed the detector for a prototype color CS camera to position three photodiodes at the correct locations to intercept each of the dispersed spectral features shown in Fig. 11(b), where a fourth detector has been placed at the position of the undiffracted grating 0th order for broadband detection. The spectral performance of the 4-channel photodetector is shown in Fig. 12 where it is assumed that silicon is used at visible and near-IR wavelengths up to 1000nm while InGaAs is used from 900-1700nm.

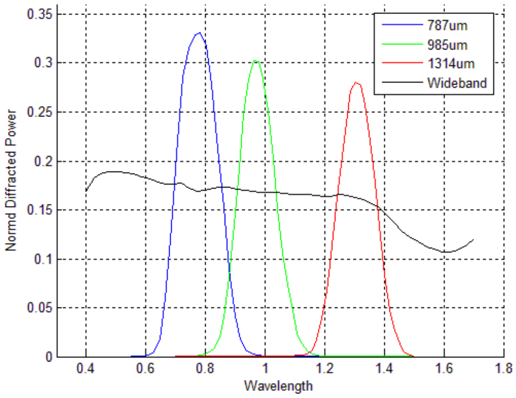

Fig. 12. Spectral performance of the multi-photodiode detector showing three wavebands of about 150 nm width plus a fourth wideband detector.

A photograph of the detector circuit board built for this design is shown in Fig. 13, along with a view of the multi-spectral camera testbed. In the testbed, the single-element detector has been removed from an existing compressive camera and replaced with a grating, a focusing lens system and detector alignment fixture.

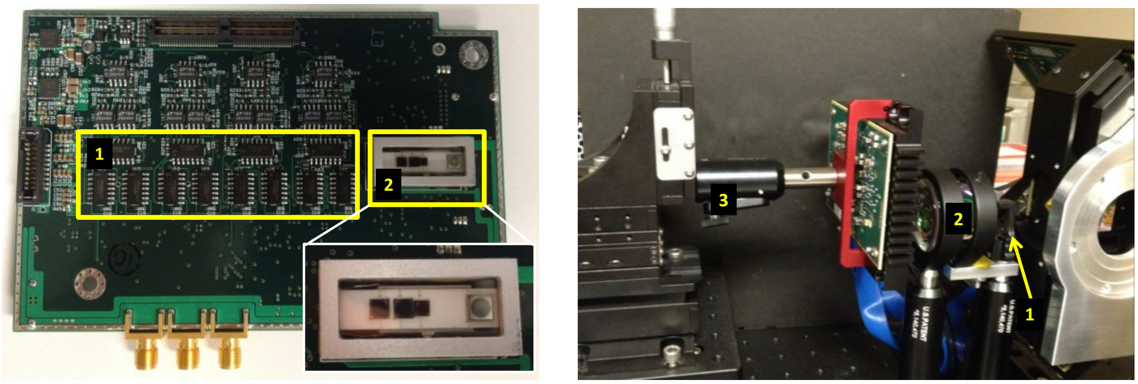

(a) (b)

Fig. 13. (a) Detector PCB front showing 1) measurement circuitry for the four signal channels, and 2) the packaged multi-die detector containing four photodiodes for detecting multi-spectral optical signals. The inset shows a close-up of the detector and its variety of photodiodes. (b) Camera testbed optical path leading up to the detector. The camera body is located far right. Component 1) is the diffraction grating located in front of 2) a two-lens system that focuses light onto the detectors. Here a single-element detector PCB is mounted on the alignment fixture (3). When complete, the new multi-element PCB will be attached to this fixture for testing.

The multi-spectral camera concept was tested by positioning a single detector at each of four spectral positions, taking measurements of the modulated image light at the focal plane and reconstructing images using CS techniques. The results of this test are shown in Fig. 14. For the tests shown here, a single detector was positioned at each location and then repositioned to the next location after the CS data was taken. Similar CS patterns were displayed on the DMD in each case and the same CS reconstruction algorithm was used to create the images in Fig. 14. In the completed multi-spectral camera, data from all spectral components will be acquired in parallel by the four-channel detector. In the mean time, these preliminary results prove that each diffracted order of the DMD contains all spatial and spectral information necessary to perform CS imaging.

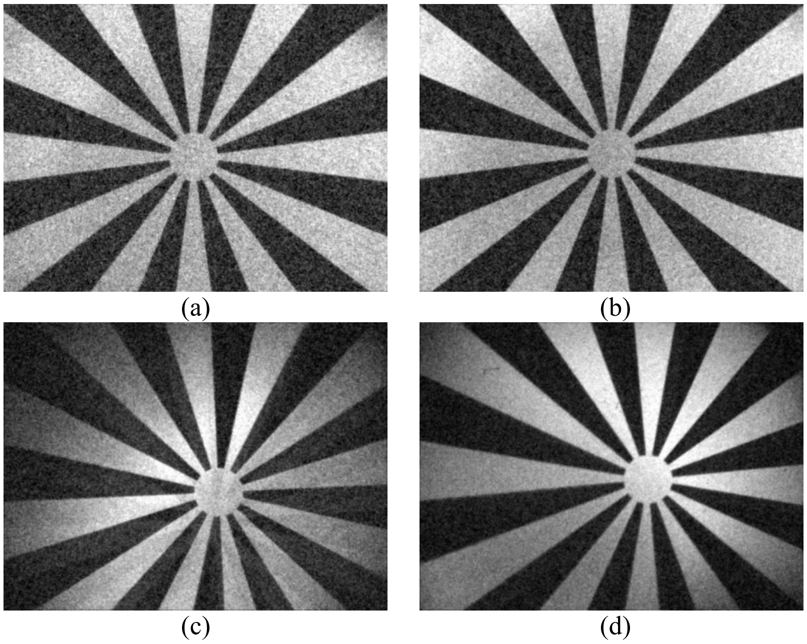

Fig. 14. Reconstructed images from the measurements taken at different wavelengths throughout the visible and shortwave infrared using the benchtop color CS camera testbed shown in Fig. 14(b). These images were measured at (a) 514nm , (b) 637nm , (c) 900nm, and (d) 1310nm.

6. SUMMARY

We have presented a simplified compressive-sensing-based multi-spectral imager architecture that utilizes both the spatial light modulation and diffractive properties of the DMD. We developed a model of how the diffractive properties of the DMD provide convenient spectral features for compressive imaging, and used the model to design a new multi-channel detector for compressive imaging. Through experiments on a testbed system, we verified that measurements made at each of these discrete spectral components will yield a full-resolution image representing the spatial information at the wavelengths associated with that component. This means that each component may be individually and independently measured and resulting images from each component may be arranged in a spectral data cube or combined to form a multi-color, full-resolution image. The number of spectral bands and their center wavelengths (in the range from 0.35 µm through 1.7 µm) can be specified by selection of diffraction grating spacing, and the number and position of the individual detectors.

In addition to experimental validation of the design, we examined the operational parameters of the architecture allowing us to understand the most critical design elements of the system. These elements can be boiled down to two physical properties of the light traveling through the camera's optical path to the detector plane: 1) the optical diffraction spot size, and 2) the spot's location on the detector plane.

7. ACKNOWLEDGEMENTS

This work was funded in part by a grant from the National Science Foundation. InView would like to thank Dr. Byron Zollars of Nanohmics, Inc. for his part in the development of models and software used in this work.

8. APPENDIX

The illumination function represented by $a(x,y)$ or $a(x')$ in the above analysis is a function of the amplitude of the image incident on the DMD and is also a function of the amplitude of the modulation pattern shown on the DMD. The far-field pattern $G(f)$ shown by Eqs. 7 and 15 contain the Fourier transform $A(f)$ of the illumination function, which was shown to be replicated at each diffracted order of the DMD. As a result, the shape and distribution of light around each order is a function of the imaging system, namely the numerical aperture of the optics imaging onto the DMD, and the modulation patterns on the mirrors. If we call the image u(x′) and the micromirror "transmission function" t(x') then $a(x') = u(x')t(x')$ and the amplitude of the far-field pattern becomes proportional to the convolution of the spectra of u and t, $U(f) \otimes T(f)$.

Figure A-1 clearly shows the effect of this convolution as the modulation patterns change from left to right from a random mirror pattern to checkerboards of different sized groups of mirrors and as the aperture of the imaging objective is closed down from the top row to the bottom row. The effect of the aperture size has been numerically modeled for the case of all mirrors on and is shown in Fig. A-2.

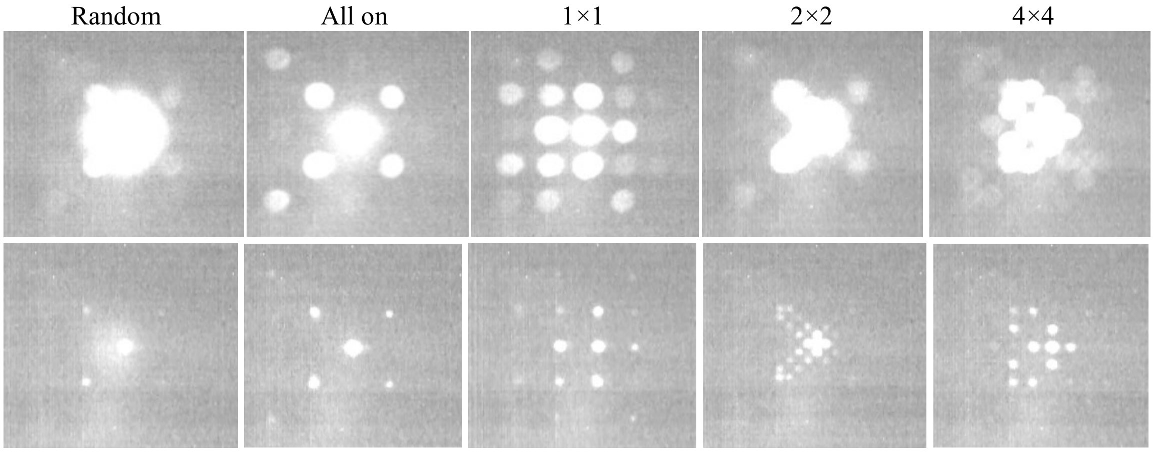

Fig. A-1. Photographs of the far-field light distribution at the focal plane of the CS camera (position 3 in Fig. 1) for illumination at 1310 nm. From right to left, the modulation pattern of micromirrors on the DMD changes from a random pattern of on and off pixels, to all on, to a 1-mirror checkerboard, 2×2 mirror checkerboard and 4×4 mirror checkerboard pattern of on and off pixels. The top row shows the case of an open imaging system aperture while in the bottom row the aperture has been closed down the smallest aperture (largest F/#) we could obtain experimentally.

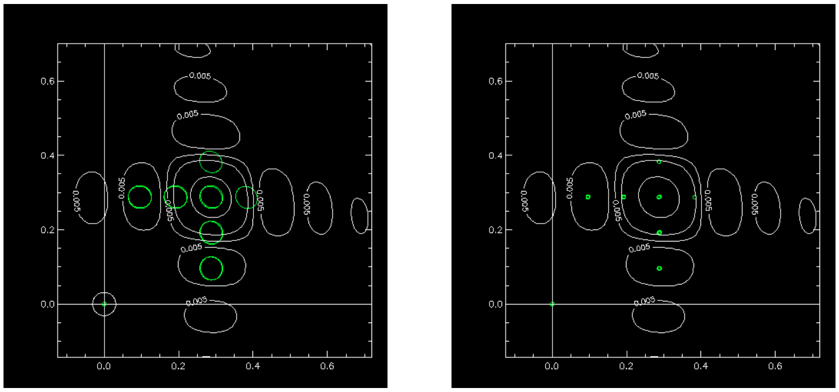

(a) (b)

Fig. A-2. Model of the diffraction pattern at the detector plane at wavelength 1310nm for an optical system at (a) F/20 and all DMD mirrors on; (b) Same case with a much smaller aperture. Note that the axes are rotated 45 degrees from the photograph of the same case (All on) in Fig. A-1.

REFERENCES

[1] Romberg, J., “Imaging via compressive sampling,” IEEE Signal Process. Mag. 25(2), 14–20 (2008).

[2] Willett, R. M., et al., “Compressed sensing for practical optical imaging systems: a tutorial,” Optical Engineering 50(7), 072601 (July 2011).

[3] Dai W, et al., “Compressive sensing DNA microarrays,” RG EURASIP J Bioinform Syst Biol., 162824 (2009).

[4] Tan, H., et al., “A computational model for compressed sensing RNAi cellular screening,” BMC Bioinformatics 13, 337 (2012).

[5] Conrad, T. O., et al., “Sparse proteomics analysis- a compressed sensing based approach for feature selection and classification of high-dimensional proteomics mass spectrometry data,” arXiv:1506.03620v1 (2015).

[6] Ganguli,S. and Sompolinsky, H., “Compresses sensing, sparsity and dimensionality in neuronal information processing and data analysis,” Annu. Rev. Neurosci., 35:485-508 (2012).

[7] McMackin, L., et al., "A high-resolution SWIR camera via compressed sensing," Proc. SPIE 8353, 835303 (2012).

[8] Tidman, J., et al., " Compact opto-electronic engine for high-speed compressive sensing,” Proc. SPIE 8856, 885616 (2013).

[9] Takhar D., et al., “A new compressive imaging camera architecture using optical-domain compression,” in Proc. Computational Imaging IV 6065, 43–52 (2006)

[10] Many recovery algorithms are available at: http://dsp.rice.edu/cs

[11] Barnard, K. J., Boreman, G. D.and Pape, D. R., “Crosstalk model of a deformable mirror-based infrared scene projector,” Opt. Eng. 33(1), 140-149 (1994).

[12] Sun, T. and Kelly, K., "Compressive Sensing Hyperspectral Imager," in Frontiers in Optics 2009/Laser Science XXV/Fall 2009 OSA Optics & Photonics Technical Digest, paper CTuA5 (2009).

[13] Magalhães F, et al., “High-resolution hyperspectral single-pixel imaging system based on compressive sensing,” Opt. Eng. 51(7), 071406 (2012).

[14]Goodman, J. W., [Introduction to Fourier Optics,] 2nd International Ed., McGraw-Hill, Boston, MA, USA, 2002.

[15] Russell, T. A., et al., “Compressive hyperspectral sensor for LWIR gas detection,” Proc. SPIE 8365, 83650C. (2012).

[16] DCLab™ diffraction software, InView Technology Corporation, www.inviewcorp.com, © 2015.

[17] Harvey, J. E. and Vernold, C.L., “Description of Diffraction Grating Behavior in Direction Cosine Space,” Applied Optics 37, 8158 (1998).